Carbon xxx (2018) xxx-xxx

Contents lists available at ScienceDirect

Carbon

journal homepage: www.elsevier.com

Development of mesopores in superfine grain graphite neutron-irradiated at high fluence☆

Cristian I. Contescu[a, *], José D. Arregui-Mena[a, **], Anne A. Campbell[a], Philip D. Edmondson[a], Nidia C. Gallego[a], Kentaro Takizawa[b], Yutai Katoh[a]

[a] Oak Ridge National Laboratory, Oak Ridge, TN, USA
[b] Tokai Carbon, Ltd., Japan

ARTICLE INFO

Article history:
Received 19 July 2018
Received in revised form 20 August 2018
Accepted 21 August 2018
Available online xxx

ABSTRACT

Microstructural changes induced by neutron irradiation of superfine grain graphite G347A (Tokai Carbon, Japan) were examined by nitrogen adsorption at 77 K and by three microscopy techniques (SEM, TEM and FIB-SEM tomography). The specimens were irradiated at doses of up to 30 dpa, covering stages before and after the turnaround fluence at three temperatures (300, 450, 750 °C) of their irradiation envelope. The initial graphite densification at low fluences did not produce any detectable effect in the pore size range (<350 nm) measured by gas adsorption. However, graphite irradiated at high fluences, after turnaround, showed severe structural changes. At all three temperatures and high irradiation fluences, gas adsorption revealed significant increase of the volume of narrow mesopores (<5–20 nm) and up to five times increase of BET surface area, both in linear relationship with the relative volume expansion. Analysis of microscopy images showed multiplication of fine macropores (>50 nm) at high irradiation fluences and more structural changes on multiple scales, from nanometers to microns. This work demonstrates the unique ability of gas adsorption techniques to analyze open pores with sizes between sub-nanometer and sub-micron in bulk nuclear graphite, with supporting microscopy results.

1. Introduction

It has been known from the time of the Manhattan Project that graphite could be used as moderator of fast neutrons in nuclear fission reactors. About the same time, it was also discovered that extended irradiation with high energy neutrons would cause dimensional and structural changes in core graphite components, with significant consequences on the properties critical to reactor operation [1]. The visible effects of neutron irradiation are dimensional changes, but inisidious degradation of thermal and mechanical properties is also very important. Despite the significant progress with characterization and first-principles modeling of irradiation-induced microstructural changes, the exact mechanism is still not clearly understood. The growing interest in development of high-temperature gas-cooled reactors (HTGR) and molten-salt reactors (MSR) stimulates more research into the microstructure of neutron-irradiated graphite used as moderator and structural material in advanced nuclear reactors (generation IV). In fact, graphite is the limiting component of some nuclear reactors' life time, while at the same time graphite maintains the fuel integrity.

Along with filler grains of synthetic graphite and pitch binder, porosity is the third important component of high density nuclear graphite. Open and closed pores represent about 18–20 vol % in graphite and as such it has an important role in ensuring the physical integrity of graphite components in the reactor. Porosity is critical for accommodating thermal expansion [2], absorbing dimensional changes caused by irradiation [3] and for withstanding large internal crystallite strains without severely deteriorating the properties (irradiation-induced creep) [4]. Porosity also affects mechanical and thermal properties, gas transport, oxidation behavior and fission products retention. Large pores deflect crack propagation, while fine pores (in smaller grain graphites) make graphite more brittle and may downgrade its thermal properties [5]. Elastic moduli decrease with an increase of pore fraction [6]. Whereas, development of porosity due to oxidation may cause a decrease of thermal conductivity [7] and significant degradation of mechanical properties [8] that may threaten the integrity of graphite components. Porosity is present in the graphite filler, in the binder, and at the filler/binder interface. The volume fraction of pores, their shape, orientation, and size distribu-

* Corresponding author.
** Corresponding author.
Email addresses: ContescuCI@ornl.gov (C.I. Contescu); ArreguiMenJD@ornl.gov (J.D. Arregui-Mena)

https://doi.org/10.1016/j.carbon.2018.08.039
0008-6223/

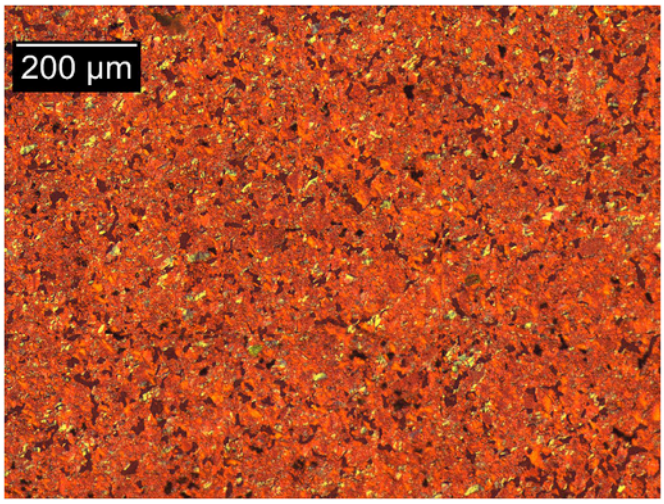

Fig. 1. Polarized light optical microscopy image of pristine superfine grain graphite G347A.

tion depend intrinsically on the raw materials, number and types of intermediate steps in the manufacturing process, and thermal history of each graphite billet [9]. Control of porosity is possible to some extent during manufacturing (through precursor selection, forming techniques, and impregnation treatments for densification). However, the porosity control techniques have limitations so that, in some sense, and with the best efforts of manufacturers, at the end "you get what you get".

Even less understood are the microstructural changes that accompany bulk volume variations caused by high energy neutron irradiation. The currently accepted views [10] [11], are that crystallites expansion along c-axis is accommodated by closing of large pores, while contraction along a-axis, which is not accommodated, causes the overall bulk shrinkage of graphite artifacts, which increases in magnitude with increasing irradiation dose. At the point of turnaround, when the accommodation pores are filled due to irradiation-induced swelling on c-direction and thermal expansion, the continuous dilation along c-axis overtakes the a-axis contraction resulting in recovery of previous shrinkage and even swelling beyond the initial volume, with severe structural damage [12]. Most information on defect evolution relies on observations made in-situ on either electron- or ion-irradiated graphites. Direct observations on *neutron*-irradiated graphite are more difficult to make, and the information available is limited. Tanabe et al. [13] obtained evidence from Raman spectroscopy on defects in, and/or between basal planes produced at early stages of neutron irradiation; their evolution caused turbulence and bending of basal planes under heavy irradiation. Using small angle X-ray scattering (SAXS), Eeles [14] identified disc-like interstitial aggregates in pile-irradiated polycrystalline graphite. Evidence from X-ray diffraction (XRD) and small angle neutron scattering (SANS) showed that lattice parameters of HOPG graphite crystallites vary by lesser amounts than the overall bulk dimensional changes [15]. Mercury porosimetry was used for pore size distribution measurements from sub-millimeters to nanometers, but there were concerns that the high pressure required to survey nanometer size pores may damage the graphite structure [16]. Electron microscopy shows interstitial defects and microcracks in specimens irradiated by neutrons [17,18], electrons [19,20,21], or ions [22], but it is difficult to assess the global contribution of these localized nanoscale defects to the large dimensional changes measured on bulk specimens. X-ray computed tomography can provide information on the connectivity and geometry of pores, but currently this technique is limited in its ability to resolve small pores in a large volume. There is a need for an analysis technique with resolution at the nano- and mesoscale, and yet capable of providing statistically significant information from bulk measurements on large (millimeter size) specimens. Gas adsorption may fill this need.

Gas adsorption techniques provide information on open pores from the sub-nanometer to sub-micron scales, but these techniques have not been used so often for characterization of polycrystalline nuclear graphite. Very recently, Jones et al. [23] used low pressure gas adsorption and He pycnometry in combination with mercury porosimetry and a modeling technique to obtain information covering four orders of magnitude between the smallest and the largest pores in graphite. Hoinkis et al. used N_2 adsorption and SAXS to analyze the change in porosity of pristine, oxidized [24], and irradiated A3-3 matrix graphite [25]. They found that irradiation at about 7 dpa (displacements per atom[1]) caused pronounced development of micropores and small mesopores, of which most were accessible to nitrogen. Banares-Munoz et al. measured adsorption isotherms of N_2 and Ar on AGOT nuclear graphite [26] and pyrolytic graphite [27] and derived textural information by comparing the isotherm shapes and the BET surface areas (calculated by the Brunauer-Emmett-Teller method) [28]. They interpreted the changes in slope of adsorption isotherms at sub-monolayer coverage as an indication for occurrence of sites with different adsorption potential on graphite (lattice defects, layer boundaries) combined with the effect of lateral interactions in the adsorbed monolayer. In continuation of this argument, Olivier and Winter [29] postulated that adsorption sites on the graphite basal plane surface are characterized by an adsorptive potential centered at 57 ± 2 K (based on N_2 adsorption at 77 K); edge sites on the prismatic graphite surface were identified with lower adsorptive potential (20–40 K) while defective sites (dislocations, surface steps) were assigned higher values (up to 80–90 K).

Further advancing the use of nitrogen adsorption at 77 K, this communication reports on a lesser known aspect of microstructural changes in neutron-irradiated superfine graphite at fluences before and after turnaround, up to (high) doses of 30 dpa. The changes in nanoporosity uncovered by nitrogen adsorption, and the associated changes in BET surface area, are supported by three microscopy techniques which provide complementary information on pores ranging from tens of nanometers to hundreds of microns. This information sheds unique light on microstructure evolution in superfine grain graphite irradiated before and after turnaround. A complementary Data-in-Brief manuscript shows video files for FIB-SEM tomography, TEM images, and gas adsorption data.

2. Materials and techniques

The material examined was superfine grain graphite G347A manufactured by Tokai Carbon Co., Ltd. by cold isostatic pressing. According to the manufacturer's website [30], G347A is obtained from coal coke filler and a pitch binder, and has a specific density of 1.85 g/cm^3. According to indirect information from literature [31], graphite G347A is isotropic, with 11 μm grain size (superfine grade) and porosity of only 12% volume. Optical microscopy imaging using polarized light supports this information (Fig. 1). The effects of neutron irradiation on this graphite's properties were reported recently by

[1] The multiplier for conversion of dose units in n/m^2 [E > 0.1 MeV] to displacements per atom (dpa) used in this work was 7.3E-26 [see T D Burchell, Fission reactor applications of carbon, in "Carbon Materials for Advance Technologies", Ed. T D Burchell, Pergamon, 1999, p.459].

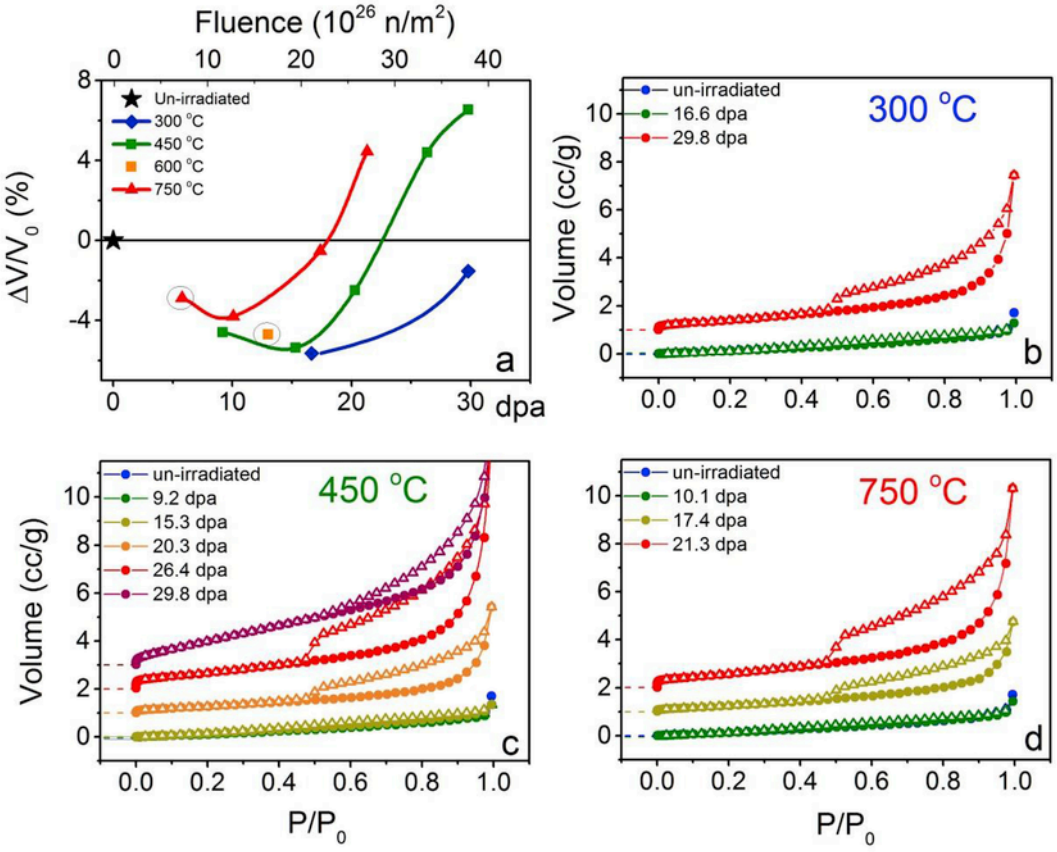

Fig. 2. Variation of relative specimens' volume as a function of irradiation fluence and temperature (a) and adsorption-desorption isotherms of N_2 at 77 K for specimens irradiated at 300 °C (b), 450 °C (c) and 750 °C (d) nominal temperatures. Two circles in (a) mark the two specimens that were not characterized by gas adsorption. The isotherms were shifted upward for clarity. (A colour version of this figure can be viewed online.)

PleIrradiation conditions and properties of G347A graphite measured by gas adsorption.

Nominal Irradiation temperature	Actual specimen temperature	Fluence $E>0.1$ MeV	dpa	$\Delta V/V_o$	S_{BET}	S_{DFT}	V_{tot}	V_{DFT}	Comments
°C	°C	10^{25} n/m^2		%	m^2/g	m^2/g	mm^3/g	mm^3/g	
none	none	none	none	none	0.86	0.57	2.64	1.55	un-irradiated reference
300	329	22.8	16.6	−5.64	0.96	0.62	1.97	1.44	turnaround
	345	40.8	29.8	−1.53	1.61	2.09	9.97	6.99	maximum swelling, still $\Delta V/V<0$
450	383	12.6	9.2	−4.59	0.96	0.56	2.08	1.36	before turnaround
	418	21.0	15.3	−5.38	1.17	0.69	2.09	1.62	turnaround
	463	27.8	20.3	−2.50	1.15	1.50	6.83	4.75	past turnaround, still $\Delta V/V<0$
	414	36.1	26.4	4.40	2.62	3.17	15.96	10.72	initial swelling, $\Delta V/V>0$
	377	40.8	29.8	6.55	5.22	3.35	16.26	10.92	maximum swelling
600	555	17.8	13.0	−4.71	n/a	n/a	n/a	n/a	dose comparison (*)
750	658	7.9	5.8	−2.89	n/a	n/a	n/a	n/a	before turnaround (*)
	610	13.8	10.1	−3.81	1.01	0.61	2.21	1.47	turnaround
	693	23.8	17.4	−0.52	1.14	1.41	5.80	4.22	dose comparison $\Delta V/V\simeq 0$
	622	29.2	21.3	4.45	2.34	2.87	12.85	8.85	maximum swelling

Note: Gas adsorption was not performed on specimens marked with asterisks (*).

Campbell et al. [32] Irradiation was performed at the High Flux Isotope Reactor (HFIR) on Oak Ridge National Laboratory (ORNL) campus. The properties characterized at ORNL before and after irradiation include volume and dimensional changes, elastic and shear moduli, electrical resistivity, equiaxial strength, thermal conductivity and coefficient of thermal expansion.

In this study, a small subset of the irradiated specimens was characterized by nitrogen adsorption at 77 K. A pristine specimen was also measured for comparison. All selected specimens were thin slabs with $48\times6\times1$ mm^3 size. They have been previously irradiated at three different nominal temperatures (300, 450 and 750 °C) and doses of up to 30 dpa, covering stages before and after the turnaround point of their irradiation envelope. The capsules used for irradiation in

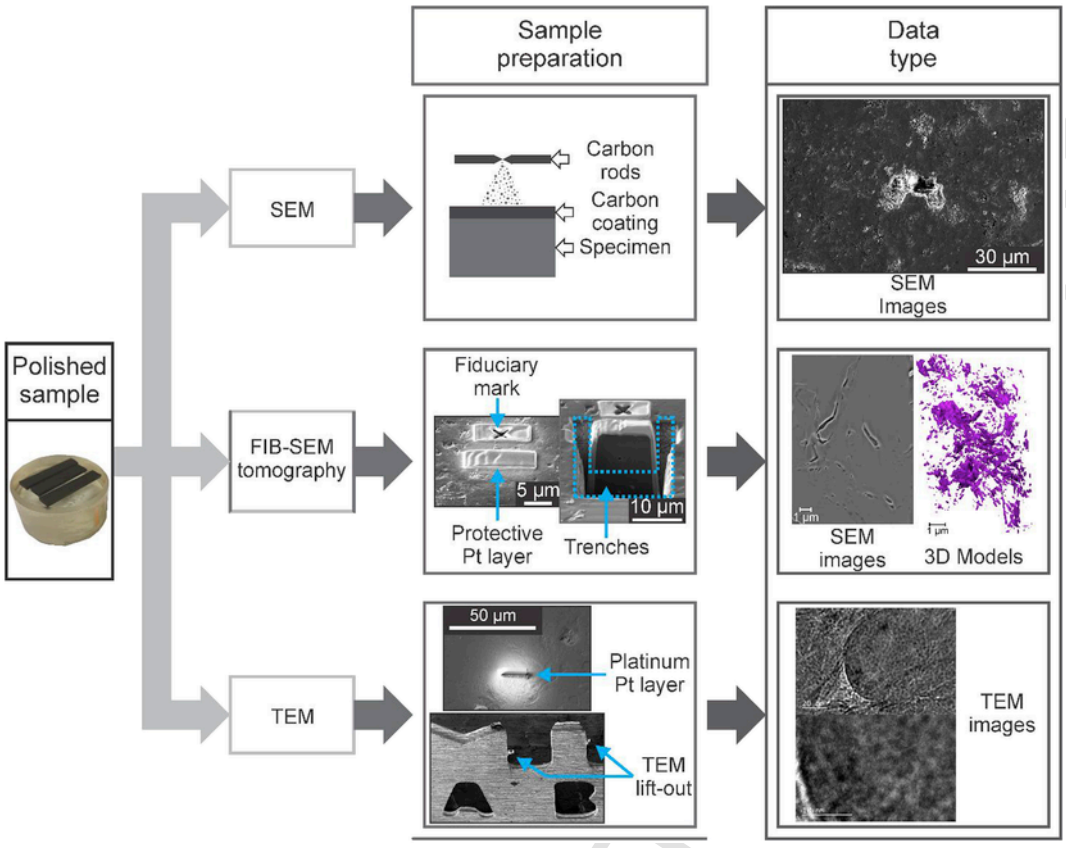

Fig. 3. Sample preparation and data acquired by SEM, FIB-SEM tomography and TEM. (A colour version of this figure can be viewed online.)

HFIR did not have active temperature control. Their temperature was varied by adjusting the composition of gas mixtures (Ar, Ne, He) in the insulating gas gap between the external housing and the inner specimen holder. These inert gases served two purposes: local temperature control amd protection against oxidation [32]. The relative variation of graphite volume with the irradiation fluence is shown in Figs. 2a and 4a. As expected, the turnaround fluence and the corresponding relative volume shrinkage decrease with the increase of irradiation temperature (Table 1).

Equilibrium adsorption/desorption isotherms of N_2 at 77 K were measured using the Autosorb 1C instrument (Quantachrome). Graphite specimens (about 0.53 g each) were outgassed for 2–3 h at 300 °C prior to measurements, except for the specimens irradiated at 300 °C which were outgassed at a lower temperature (265 °C) to prevent annealing of irradiation damage during outgassing. A total of 117 data points were collected during adsorption and desorption, with equilibration times of at least 5 min. Table 1 shows the actual irradiation temperatures and irradiation fluences for the specimens characterized by N_2 adsorption, and all properties calculated from these measurements. The total pore volume (V_{tot}) was calculated from the largest amount of N_2 adsorbed at $P/P_o \sim 0.995$. This is the cumulative volume of all open pores with characteristic dimension $\lesssim$350 nm. Note that two specimens listed in Table 1 and represented in Figs. 2a and 4a were actually not measured by gas adsorption.

To identify the pore structure and its connectivity, an additional subset of samples used for equibiaxial strength measurements and irradiated in the nominal range of 450 °C were prepared for microscopy analysis. A trio of microscopy techniques was used, that includes Scanning Electron Microscope (SEM), Transmission Electron Microscopy (TEM), and an original combination of Focused Ion Beam (FIB) and SEM – the FIB-SEM tomography, Details of sample preparation and corresponding data examples are summarized in Fig. 3 and described below. All sample preparation and microscopic imaging was performed in the Low Activation Materials Development and Analysis (LAMDA) laboratory at ORNL.

2.1. Sample polishing

The samples used for this research were embedded in epoxy pots, in order to prevent contamination of equipment, and mechanically polished. Polishing followed a sequence of steps with successively finer grit silicon carbide polishing paper, followed by a final vibratory polish with a 1 µm diamond suspension.

2.2. SEM

The samples, in the polishing mounts, where coated with a thin layer of carbon (~1–10 nm) deposited with a carbon coater to improve the conductivity of the sample. All samples where imaged with a FEI Versa 3D Dual BEAM at an electron beam acceleration voltage of 5 kV.

2.3. FIB-SEM tomography

Two protective layers of platinum were deposited, of which the first layer was placed at the area of interest and the second layer was used to mill a fiduciary mark serving as reference during the imaging process. Trenches were milled around the area of interest to improve the imaging conditions and to reduce redeposition of material. The resolution and scanned volume by this technique are summarized in

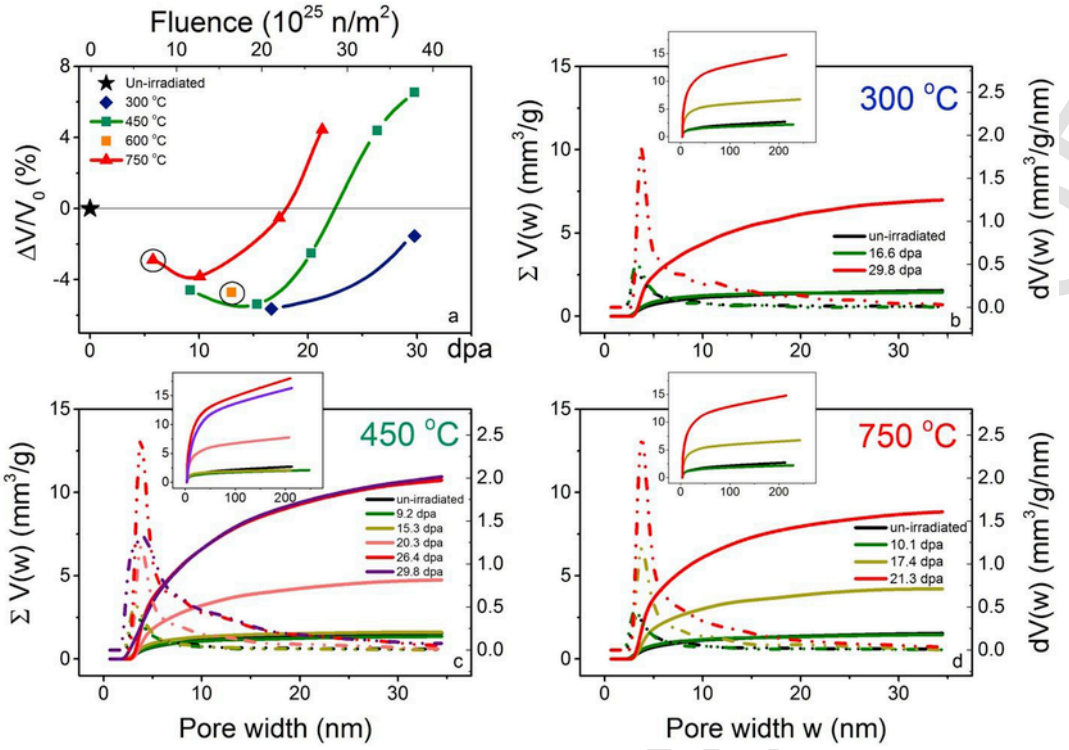

Fig. 4. Variation of relative specimens' volume as a function of irradiation fluence and temperature (a); cumulative (solid lines, left axis) and differential (broken lines, right axis) distribution of pore volumes by pore widths for specimens irradiated at 300 °C (b), 450 °C (c) and 750 °C (d) nominal temperature. Insets show cumulative mesopore distributions ($\Sigma V(w)$, mm^{3}g^{-1}) calculated from desorption branches of isotherms using the BJH method (same axes units as in the main graphs). Two circles in (a) mark the two specimens that were not characterized by gas adsorption. Note that BJH analysis explores broader pore size ranges (up to ~275 nm) and returns larger cumulative pore volumes. (A colour version of this figure can be viewed online.)

Table 2
Irradiation conditions (at 450 °C nominal irradiation temperature) and properties of G347A graphite measured by FIB-SEM.

Sample	Number of slices/images	Dimensions (μm)	Scanned volume (μm^3)	Voxel resolution (μm)
Control sample	164	11.45 × 15.98 × 2.44	447.36	0.027 × 0.029 × 0.015
15.3 dpa	119	7.48 × 16.54 × 1.78	140.72	0.016 × 0.021 × 0.015
26.4 dpa	252	10.04 × 13.29 × 3.78	504.37	0.018 × 0.026 × 0.015

Table 2. A sequential process was used between imaging and milling the material, with images taken at 5 kV electron beam acceleration voltage. Conditions for the ion milling procedures were 5 kV for the acceleration voltage and a current of 1 nA. This part of the study was performed in a FEI Versa 3D Dual BEAM using the FEI software Auto Slice and View G3 version 1.4.1.9. Digital 3D reconstructions of the porosity and analysis were conducted with Avizo Fire version 8.1.0.

2.4. TEM

The following TEM lift-out procedures were followed to produce the specimens. Initially a platinum layer was deposited to protect the surface of the region of interest. After this, step trenches were milled around the sample with ion beam, at voltage and current combination of 30 kV–15 nA. Then skirts were shaped around the trenches with lower current and voltage (30 kV – 5 nA). Subsequently, undercuts were produced to detach lamellae from the bulk specimen (30 kV–3 nA). In the final steps the lamellae were welded and thinned with the ion beam to produce transparent electron samples. TEM studies were conducted in a JEOL-2100 F TEM at an acceleration voltage of 200 kV, and all images were taken in bright field mode. Several precautions where taken to reduce the possible damage produced by the electron beam, among them the reduction of the intensity of the electron beam and decrease of the exposure time during the imaging procedures. As a result no amorphization was observed during the acquisition of the images.

3. Results

3.1. Adsorption isotherms

Fig. 2b–d shows nitrogen adsorption-desorption isotherms at 77 K for specimens irradiated at various fluences, at three (nominal) irradiation temperatures. Some plots were shifted upwards on the vertical axis for clarity, but the new positions of shifted baselines are indicated for each. It is immediately apparent that the unirradiated graphite and the specimens irradiated before turnaround show very little adsorption. The isotherms of un-irradiated graphite and graphite irradiated at low fluence are type II. This type of isotherms is characteristic to nonporous materials that allow unrestricted multilayer adsorption to occur at high P/P_0 (relative pressures). Irradiation before the turnaround fluence at each temperature (~16.6 dpa at 300 °C; ~15.3 dpa at 450 °C; ~10.1 dpa at 750 °C) irradiation does not cause

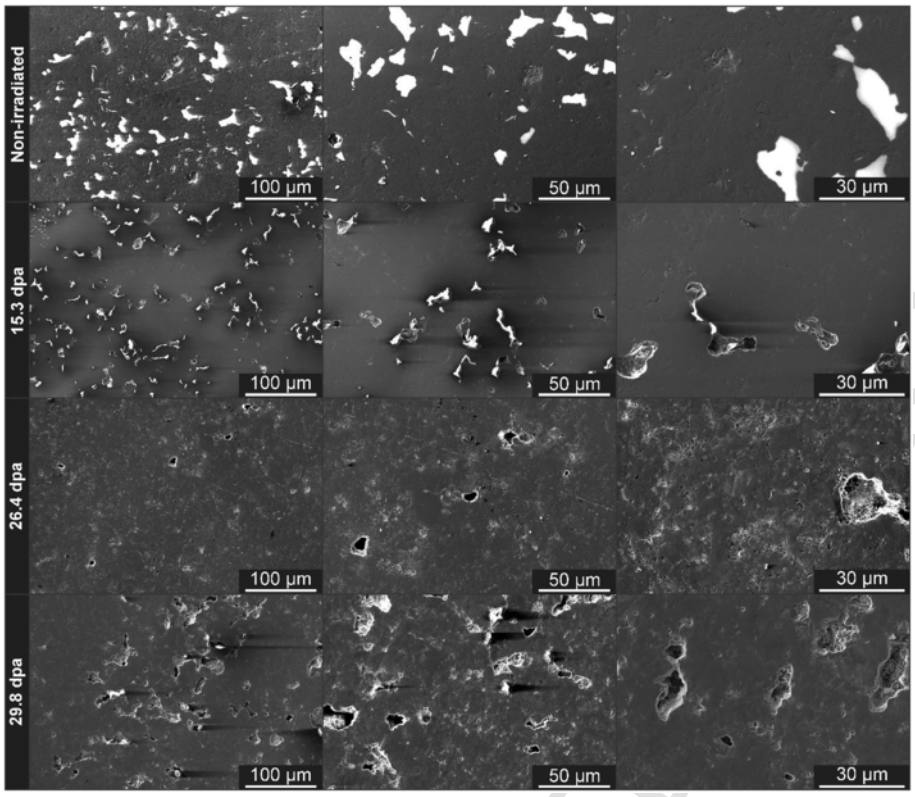

Fig. 5. SEM images of non-irradiated and samples irradiated at 450 °C (nominal). Pores may appear as white regions due to charging effects. (A colour version of this figure can be viewed online.)

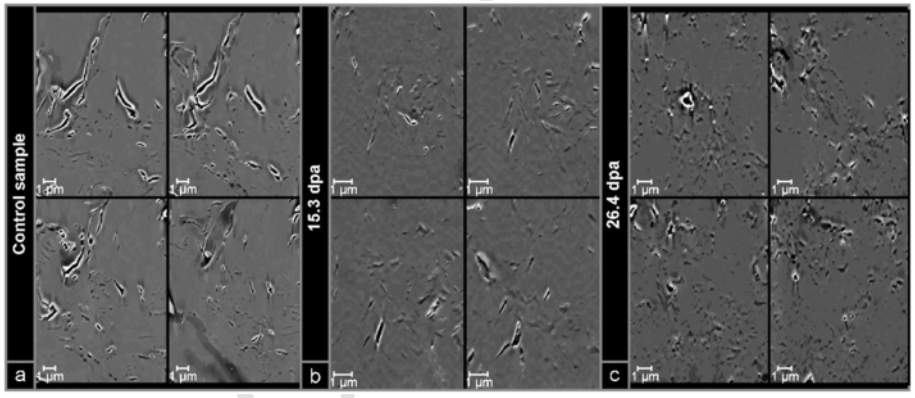

Fig. 6. FIB-SEM tomography images of non-irradiated and samples irradiated at 450 °C nominal temperature. Images were taken from the same area, just at different depths.

visible changes in nitrogen adsorption isotherms, which are indistinct from that of the un-irradiated graphite. However, after the turnaround fluence the isotherms show gradually increasing differences (hysteresis) between adsorption and desorption branches. Hysteresis is caused by differences between capillary condensation and evaporation of liquid nitrogen in mesopores (2–50 nm). With a closure point at the typical values of 0.42 P/P_o the hysteresis shapes belong to H3 class, which characterizes aggregates of plate-like particles [33]. The only exception is the sample irradiated at 450 °C and 29.8 dpa, for which hysteresis has a less defined closure point and its shape is closer to type H4 which is observed for slit-shaped pores found in activated carbons [33].

3.2. Surface area

The total surface area exposed by open pores was calculated using the BET equation [27].

$$\frac{P/P_0}{W\left(1-P/P_0\right)} = \frac{1}{W_m C} + \frac{C-1}{W_m C}\left(\frac{P}{P_0}\right)$$

where W is the amount per unit mass adsorbed at pressure P, W_m is the monolayer capacity, P_0 is saturation vapor pressure at the adsorption temperature, and C is a constant that varies exponentially with

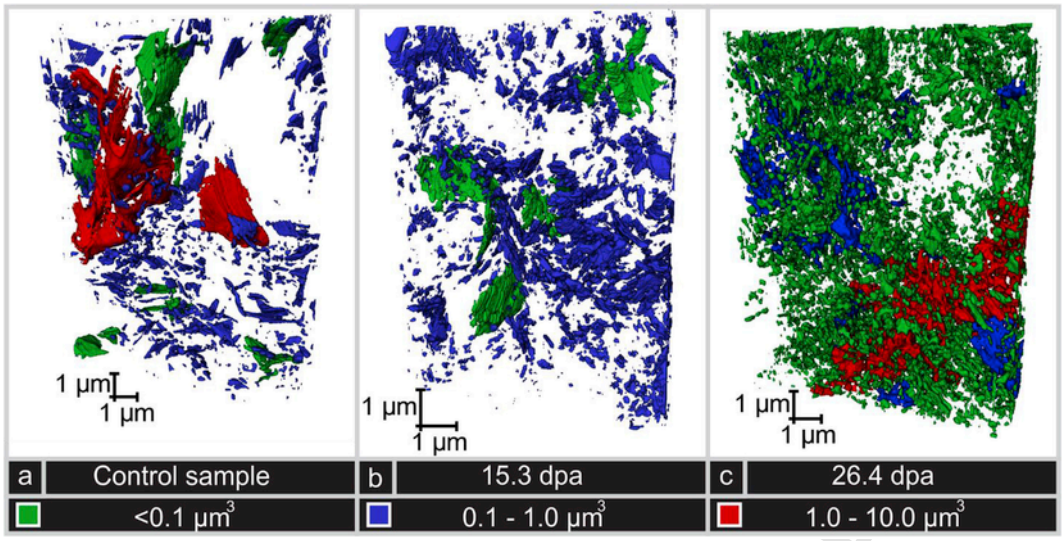

Fig. 7. Reconstructions from FIB-SEM images of non-irradiated and irradiated samples. The color code for pore sizes is the same in all three images. (A colour version of this figure can be viewed online.)

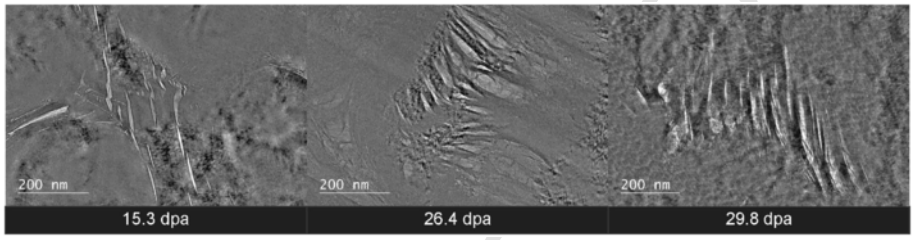

Fig. 8. Low magnification TEM images of samples irradiated at 450 °C nominal temperature. (A colour version of this figure can be viewed online.)

the adsorption energy in the first monolayer. Plots of $1/\left[W\left(\left(P_o/P\right)-1\right)\right]$ versus P/P_0 were linear for $0.15<P/P_0<0.25$, with slope s and intercept i. Selection of the data points for the BET fit was made according to recommendations by Rouquerol [33]: in the continuously increasing range of $W(1\text{-}P/P_0)$ plots versus P/P_0 but not beyond the maximum, and such that the intercept was always positive. The monolayer saturation volume was calculated as $W_m = 1/(s+i)$ and the total surface area was obtained from $S_{BET} = W_m \bar{N} A_s / \bar{M}$ where $\bar{N}$ is the Avogadro number, A_s is the cross-sectional adsorbate area (16.2 Å^2 for N_2 molecules), and $\bar{M}$ is the molecular weight of nitrogen. The S_{BET} values are listed in Table 1. The C constants were small (2–5) for the un-irradiated graphite and for specimens before turnaround, and larger (20–28) for specimens irradiated after turnaround. It can be concluded that the adsorption energy is higher for mesoporous specimens with hysteretic isotherms, produced by irradiation at high doses. This is an indication of higher adsorption potential for irradiated sample, which may have been caused by development of surface defects (edges, kinks, pits, dislocations etc). [34] [35].

3.3. Micropores and mesopores analysis by the density functional theory method

Density functional theory (DFT) analysis is the most advanced method for interpretation of gas adsorption data. It is based on microscopic representations of adsorption in solid material's pores, and uses proper gas-solid and gas-gas interaction potentials and statistical thermodynamics methods. DFT analysis provides a comprehensive description of adsorbed phase densification in the pore system, as a function of pore size, temperature and pressure. The atomic structure (roughness) of pore surfaces is accounted for in the quenched surface (QSDFT) variant of this analysis method. The results are customized for various pore geometries and specific adsorbate – adsorbent pairs. However, the pore size range analyzed by DFT method is limited to the maximum range of fluid-fluid and fluid-solid molecular interactions. Because of short interaction ranges, pores wider than about 35 nm are regarded as flat surfaces.

The calculation of size distribution in open porosity of irradiated specimens was done by the QSDFT method applied to N_2 adsorption on graphite. The best fit was obtained with slit-shaped carbon pores having rough surfaces (QSDFT equilibrium model). Fig. 4 b-d show cumulative ($\Sigma V(w)$, mm^{3}g^{-1}) and differential (d$V(w)$, mm^{3}g^{-1}nm^{-1}) distributions of pore volume (V, mm^{3}g^{-1}) versus pore width (w, nm) for specimens irradiated at three temperatures. For ease of comparison, Fig. 4a repeats the volume variation plots versus irradiation dose from Fig. 2a. The plots show that the changes in adsorption isotherms observed after the turnaround are caused by the development of mesopores (>2 nm). The cumulated volume of new pores increases with the fluence at each temperature. The differential distributions show that mesopores contribution is greater in the size range of 2–10 nm. No micropores (<2 nm) were observed from N_2 adsorption results after irradiation. This contrasts with the development of both micropores and mesopores reported for oxidized and neutron-irradiated (6–7 dpa at 850–950 °C) carbon matrix (A3-3), a component of TRISO fuel in HTGR [25]. The cumulated pore volume and surface

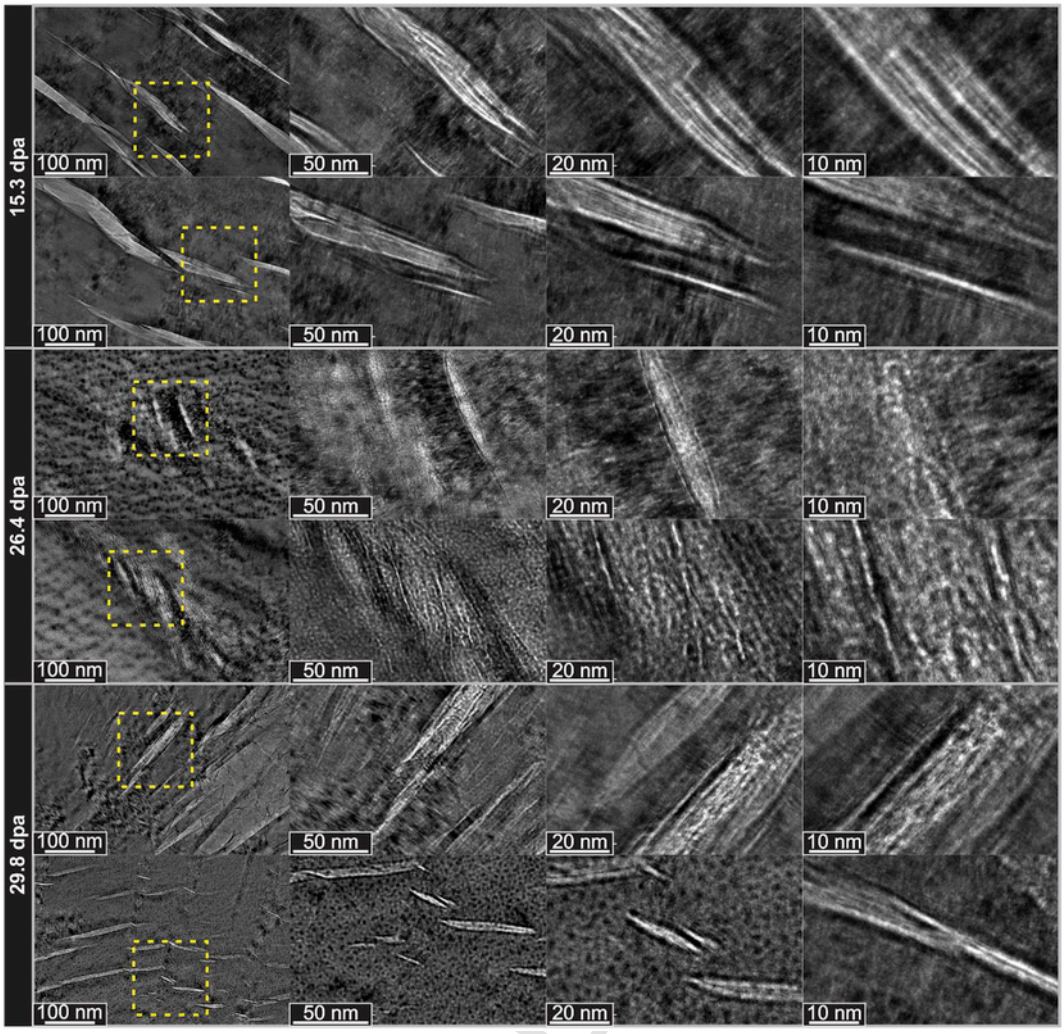

Fig. 9. TEM images of samples at irradiated 450 °C nominal temperature. (A colour version of this figure can be viewed online.)

area obtained by DFT calculations (pores < 35 nm) are also shown in Table 1.

3.4. Mesopore analysis by the BJH method

The Barrett-Joyner-Halenda [36] method (BJH) for pore size analysis of mesoporous materials is based on the modified Kelvin equation, which relates pore condensation pressures with pore diameters and the surface tension of liquid nitrogen:

$$ln\frac{P}{P_0} = -\frac{\gamma V_L}{(RT)}\left(\frac{1}{r_1}+\frac{1}{r_s}\right)$$

where γ and V_L are the surface tension and molar volume of liquid nitrogen, and r_1 and r_2 are the two curvature radii of the liquid-gas nitrogen interface at equilibrium. The contact angle is assumed zero (perfect wetting). This macroscopic classical thermodynamic model is limited by the assumption that the surface tension in a narrow pore is the same as the bulk fluid's surface tension. However, BJH method explores a range of pore sizes (up to 250–275 nm) broader than that of DFT calculations. The insets in Fig. 4b–d shows cumulative pore distributions calculated by the BJH method from the desorption branch of isotherms (Fig. 2). The agreement with the DFT calculations is fair in the range of narrow mesopores. Both sets of results show that the range of pore sizes affected by irradiation is limited to at most 20 nm, with the largest changes occurring in lower mesopores (2–10 nm).

3.5. Imaging of mesopores and macropores

The pore morphology of a control sample and samples irradiated at 450 °C (nominal temperature) was characterized through SEM, FIB-SEM tomography and TEM, as described in the methodology section. These techniques were combined to investigate the geometry of mesopores (2–50 nm) and macropores (>50 nm).

Fig. 5 compares SEM micrographs of polished surfaces of non-irradiated and irradiated samples. This data set allows to compare the structure of macropores over relatively large areas. It is seen from Fig. 5 that fine pores can be observed at high magnification in the samples irradiated at the largest doses (26.4 and 29.8 dpa). The presence of these pores may be expected as these samples would have surpassed the turnaround point.

Further analysis was performed with FIB-SEM tomography. Fig. 6 shows representative images produced with this technique and Fig. 7 presents 3D models created from each data set, as well as the pore

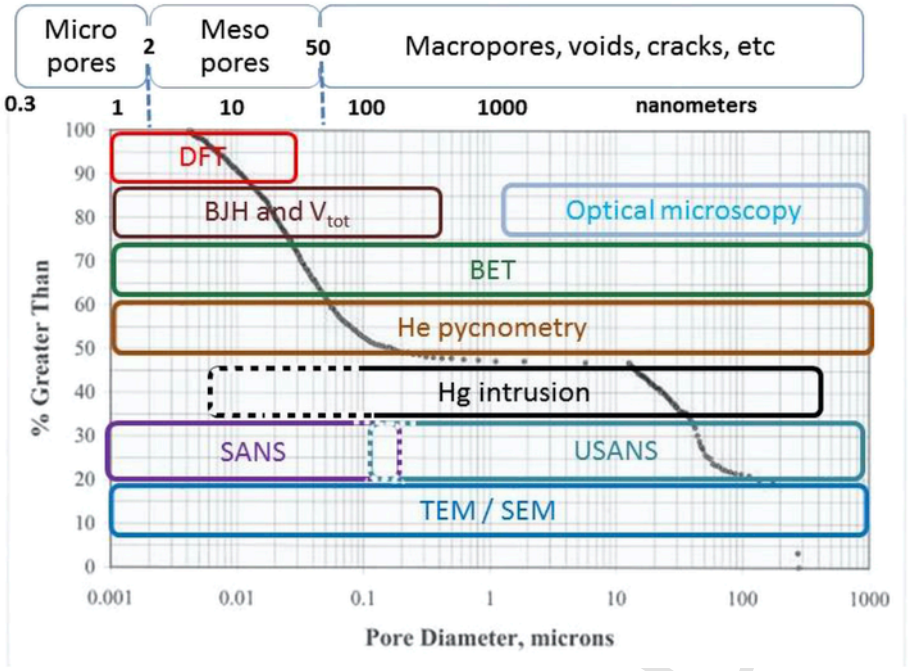

Fig. 10. Size range limitations and specific information obtainable from various experimental techniques for porosity characterization. The background plot is the cumulative pore volume distribution of a commercial medium grain graphite with bimodal porosity, measured by mercury intrusion. The top scale shows the pore classification according to IUPAC, as used for gas adsorption data. (A colour version of this figure can be viewed online.)

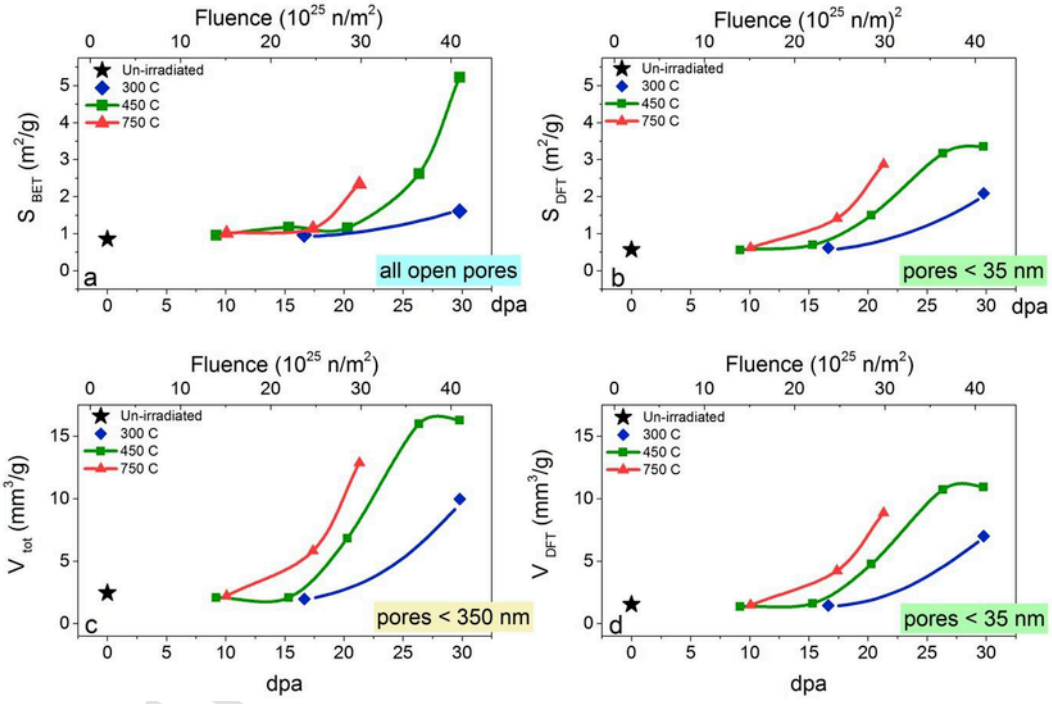

Fig. 11. Variation of BET surface area of all pores (a), DFT surface area of mesopores < 35 nm (b), total pore volume of pores < 350 nm (c) and DFT pore volume of pores < 35 nm (d) as a function of irradiation fluence and temperature. (A colour version of this figure can be viewed online.)

classification by volume. As with the previous SEM data set the highest number of pores can be observed for the sample irradiated at 26.4 dpa (Fig. 7c). The increase of irradiation dose produces significant development of pores with volume <0.1 μm^3. Closer inspection of Fig. 6c shows the presence of shallow or semi-filled pores that were found through the investigated volume.

A more detailed account of the pore morphology in irradiated samples is given by TEM images shown in Figs. 8 and 9. The first set

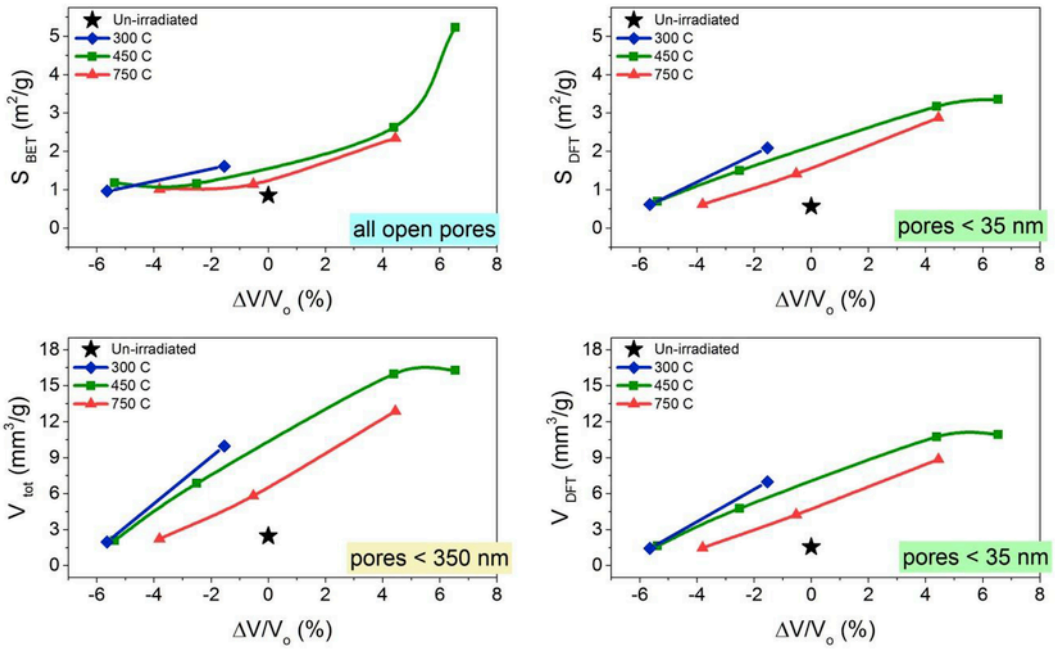

Fig. 12. Variation of BET surface area of all pores (a), DFT surface area of mesopores < 35 nm (b), total pore volume of pores < 350 nm (c) and DFT pore volume of pores < 35 nm (d) as a function of relative bulk volume changes and temperature. (A colour version of this figure can be viewed online.)

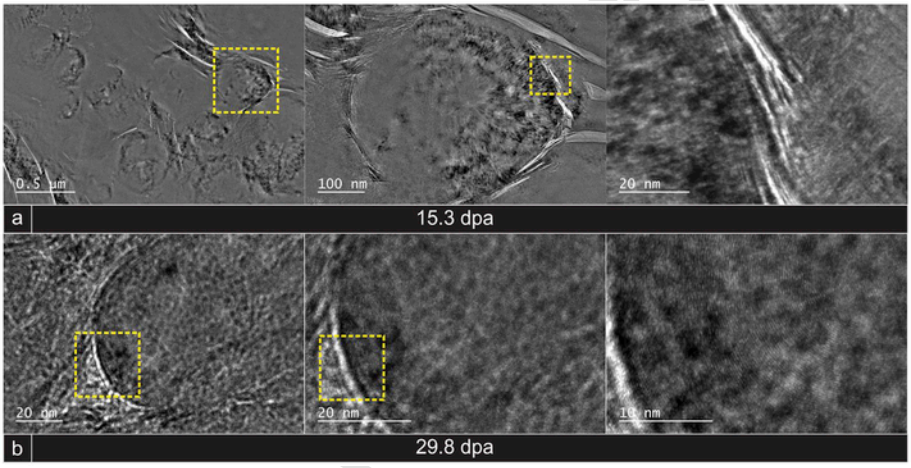

Fig. 13. Examples of irradiated QI particles in samples irradiated at 450 °C (nominal temperature).

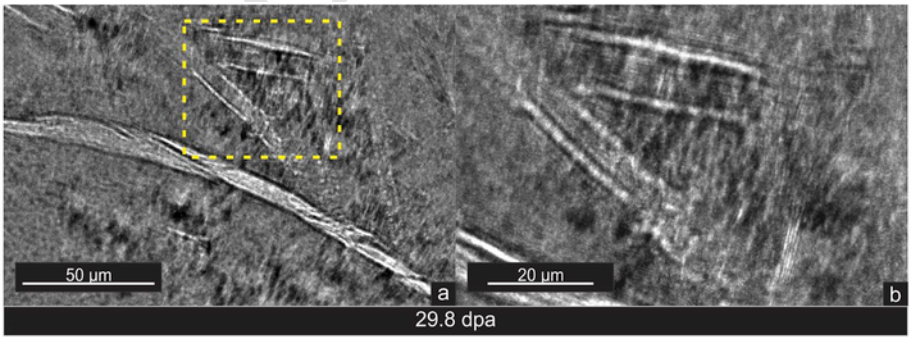

Fig. 14. Examples of interlayer splitting of crystallites.

of TEM images (Fig. 8) helps identify pores that cover significant areas around the sample. Fig. 9 helps identify details that cannot be captured at lower magnification, such as the alignment of basal planes around and inside the pores. Interestingly, the pores imaged in this study indicate the presence of materials inside the pores (Fig. 9) as was also shown by FIB-SEM tomography data.

4. Discussion

Interpretation of gas adsorption results must consider which type of information is specific to various ranges of pore size (Fig. 10). This limitation is inherent to the nature of the adsorption process and to premises of each model used for calculations. The BET surface area (S_{BET}) represents the total area of all internal surfaces in open pores, from micropores (<2 nm), through mesopores (2–50 nm) and up to macropores (>50 nm). It is calculated from the gas adsorption capacity of the first monolayer (W_m) based on the multilayer adsorption model of Brunauer, Emmett and Teller [28]. The total pore volume V_{tot} is calculated from the volume of liquid nitrogen condensed in pores at the highest relative pressure used in the test. Only pores smaller than about 350 nm are included in this measurement, because liquid nitrogen does not develop meniscus in larger pores, voids or cracks in graphite. The same range of pores is analyzed by the BJH method, which uses macroscopic models of condensation and evaporation in/from large pores; however, the BJH method is less accurate for micropore analysis. The DFT method bridges the range of micropores and that of narrow mesopores (up to about 35 nm). The cumulative pore volume (V_{DFT}) and surface area (S_{DFT}) obtained by this method are therefore a fraction of the total pore volume determined from condensation (V_{tot}) and of total BET surface area (S_{BET}). Moreover, V_{tot} measured by liquid nitrogen condensation may be smaller than the total volume of open pores, cracks and voids in graphite that is measured by helium pycnometry and mercury intrusion. There is a small range of narrow mesopores (up to about 35 nm) where information from mercury porosimetry and gas adsorption pore analysis overlaps (and in some cases [37] correlate with each other). However, there are concerns that the high mercury pressure needed to access pores smaller than about 80 nm may damage the graphite microstructures and produce misleading results [38]. Gas adsorption remains therefore a method reliable and affordable for characterization of open nanopores.

Figs. 11 and 12 show the variation of S_{BET}, S_{DFT}, V_{tot}, and V_{DFT} with fluence and relative volume variations. Some interesting observations are evident when these data are compared with the volume change plots in Fig. 2a (or 4a). Data before the turnaround point are available only for one specimen (9.2 dpa at 450 °C) but data near the turnaround point are also available at all three irradiation temperatures. All plots in Fig. 11 show that specimens irradiated before turnaround have surface areas (S_{BET}, S_{DFT}) and pore volumes (V_{tot}, and V_{DFT}) equal to those of the un-irradiated graphite. Irradiation before turnaround does not cause detectable changes in the graphite fine texture investigated by gas adsorption. In contrast, irradiation after turnaround causes sizeable texture modifications at all three temperatures. In this range all porosity properties increase with rates of change that depend on irradiation temperature as 300 °C < 450 °C < 750 °C. The plots in Fig. 12 emphasize the same trend: The graphite densification before turnaround does not affect the fine texture measured by gas adsorption. However, starting with the turnaround point (lowest irradiation dose at 300 and 750 °C, and second lowest at 450 °C) both surface areas and pore volumes increase, almost linearly, with the bulk volume expansion. There seems to be little difference in S_{DFT}, V_{tot}, and V_{DFT} between the two samples irradiated at the highest dose at 450 °C, while S_{BET} increases by a factor close to two.

The fact that specimens irradiated before turnaround show no detectable changes in gas adsorption properties when compared with the unirradiated material seems counter intuitive, since graphite irradiated at these low doses undergoes significant volume shrinkage. The explanation is simple when considering the pore size range measured by gas adsorption (Fig. 10). It is currently accepted that graphite crystallite expansion along *c*-axis is absorbed by accommodation pores, while shrinkage along the *a*-direction causes the overall negative volume changes. Accommodation pores of various types (gas entrapment, thermal cracks, and unfilled volumes) are visible by optical and electron microscopy and may represent a significant fraction of total porosity, but if their size is larger than about 359 nm (0.35 μm), condensation of liquid nitrogen is not possible. Even if gas accessible, these pores are not recorded as part of V_{tot}. Because of their large size, the internal surface of these macropores, voids and cracks contribute very little to S_{BET}, which is dominated by contributions from narrower pores. Thus, dimensional shrinkage and porosity filling before turnaround is not seen as a drop of S_{BET}. After closure of most accommodation pores, expansion along *c*-axis dominates over shrinkage along the *a*-directions and the net effect is volume expansion after turnaround. The results presented here show that volume changes after turnaround are accompanied by development of mesopores. These new pores have sizes in the range accessible to gas adsorption and their multiplication and growth (in number and total volume, but not in size) is recorded by the increase of all porosity parameters (Fig. 11) at rates almost proportional with the fluence (Fig. 12).

Typical coherent domains of graphite crystallites extend over several tens of nanometers (e.g. stack height l_c = 15–60 nm and stack width l_a = 25–60 nm) [39]. These dimensions are larger than the average width of mesopores detected by gas adsorption. Although the pore geometry is different in the DFT (slit shape) and BJH (cylinder) models used for these calculations, both models suggest that the mesopores widths are distributed narrowly between 5 and 15 nm (Fig. 4). The microstructure changes found for this superfine grain graphite (11 μm grain size) may not necessarily be expected for graphite of larger grain size. To the best of the authors' knowledge there is only one literature report by Hoinkis et al. [25] where N_2 adsorption was measured on Matrix A3-3 carbon after oxidation and irradiation (7 dpa at 950 °C). The Matrix carbon is a component of TRISO nuclear fuel, obtained from a mixture of synthetic graphite, natural graphite, and glassy carbon formed from the phenolic resin binder at the highest temperature (1800 °C) allowed for treating nuclear fuel, Neutron irradiation caused significant increase of mesopores and development of a large hysteresis but had little impact on BET surface area. This behavior was in bold contrast with the effect of oxidation by CO_2 which produced both numerous micropores and mesopores and a very large increase of BET surface area [25]. The irradiation effect reported by Hoinkis et al. agrees with the observations from this work. However, gas adsorption data by themselves are not sufficient for proposing a mechanism. Microcracks are always present in un-irradiated graphite. They vary in width (2–200 nm) and length (up to 10 μm) and can be classified as inter- and intra-granular [18]. The latter are usually lenticular in shape and parallel to basal planes of crystallites (Mrozowski cracks). Wen et al. [40] and Freeman et al. [18] obtained TEM evidence that some microcracks (<100 nm) contain low-density, amorphous carbon. Karthik et al. [17] showed that microcracks parallel to the basal planes were present in both filler and binder of grades IG-110 (fine grain) and NBG-18 (medium grain) after neutron irradiation at low dose (<2 dpa; $\Delta V/V_0$ about - 1%). At

higher doses and larger volume variations (<7 dpa, $\Delta V/V_0$ about -4%) some filler particles still contained microcracks (like in the un-irradiated material) while others showed crack closing and crystallite swelling.

One striking effect reported by Karthik et al. [17] is densification and shrinking of quinoline insoluble (QI) particles in the binder which leads to microcracks at the interface between shrunk QI particles and the surrounding matrix. Fig. 13 presents further evidence of the densification of QI particles in this superfine graphite grade. The separation distance between parallel basal planes in this particular QI particle was 0.28 nm, a reduction 13% in comparison to the original unirradiated spacing (0.335 nm). It appears that the changes of crystalline structure of QI particles affect the surrounding areas, causing cracking and debonding in the binder phase due to their shrinkage. Furthermore, the QI particles realign forming perfect concentric rings as can be seen in the high magnification sections of Fig. 13a and b. Moreover, the aspect of the QI particles appear to drastically change from rosette structures found in non-irradiated and at low neutron irradiated samples reported by Karthik et al. [17] and März et al. [41] to the recrystallized structures found at high irradiation doses (Fig. 13).

It is very hard to find in the literature any microstructure information on nuclear graphite irradiated at doses exceeding 10 dpa. The data reported in this paper are unique because they shed light on the pore structure of graphite irradiated at high fluences before and after the turnaround point, and for demonstrating the usefulness of gas adsorption as a characterization technique. Even TEM techniques cannot easily resolve micropores, as difficulties of faithfully imaging at this length scale may arise because of sample thickness effects and instrument capabilities.

The novel information is that graphite swelling after turnaround, back to the initial volume, and above it is accompanied by severe structure changes manifested as a significant increase of surface area and pore volumes in the range of narrow mesopores (5–20 nm). This effect can be specially observed in Fig. 7c as many pores start to be more prominent at higher doses. Although the limited information available at this time is not sufficient for proposing a mechanism, a few suggestions offered below may initiate the discussion. If irradiation causes some material transfer [18], then the mesopores may have been formed by opening of pre-existing microcracks in the filler, as observed by TEM at lower fluence [17], or by removal of disordered carbon from partially filled microcracks present in un-irradiated graphite. This fact is suggested by Fig. 9, as it shows the complex structure of pores, which in some cases still retain some material. However, these local microstructural transformations cannot cause by themselves five times increase of BET surface area (Fig. 5). It is more tempting to assume that the increase in porosity is in fact caused by formation of new mesopores (microcracks). Proof of this might be the development of small pores found in the 3D FIB-SEM reconstruction (Fig. 7c) and in the formation of cracks around the contour of QI particles (Fig. 13). The new mesopores may also appear inside graphite crystallites through dissimilar expansion of interlayer spacing and eventually splitting of crystallites along their basal planes as is illustrated in Fig. 14.

Support for this mechanism was provided by Gallego et al. [15] [42], who found evidence for delamination and splitting of irradiated HOPG crystallites from recent SANS measurements. Similar changes may also occur in irradiated polycrystalline graphite. It might be possible that internal stresses that grow even stronger after closing of accommodation pores produce cleavage or slippage between twin crystallites conjoined by parallel basal plane surfaces. The new pores formed in the above situations would have smooth internal surfaces of basal plane type and would be more energetically stable. Another possibility is that the new pores develop solely in the binder. The TEM study by Karthik et al. [17] of NBG-18 and IG-110 graphites irradiated at 7 dpa and the TEM data presented therein documented densification and radial shrinkage of QI particles in the pitch binder along with emergence of new microcracks at the interface with the surrounding binder matrix (Fig. 14). A fourth possibility is that shrinkage along the *a*-direction would disjoin neighboring crystallites aligned at their prismatic faces. In the latter two scenarios the internal surfaces of the new pores would be rough and more energetically unstable. Gas adsorption may help distinguish between these scenarios. It is known that the submonolayer adsorption of some inert gases (Kr, N_2, Ar) on energetically- and structurally-uniform surfaces exhibits characteristic 2D phase changes [43]. In particular, Kr adsorption at 77 K on high temperature graphitized carbon black occurs by a layer-by-layer mechanism, giving rise to type VI isotherms [44]. Investigation of gas adsorption (N_2, Kr, Ar, CO_2) on graphites of various grain sizes, irradiated before and after turnaround, may help clarify some hidden aspects of irradiation damage evolution at nano- and mesoscale. New gas adsorption measurements on irradiated nuclear graphite are currently being pursued in our laboratory.

5. Conclusion

The experimental techniques used in this study, nitrogen adsorption and the electron microscopy trio (SEM, FIB-SEM and TEM), complement each and provide new information on the structural changes caused by neutron irradiation of superfine grain graphite before and after turnaround. As a bulk characterization technique for graphite, gas adsorption measures total BET surface area of all gas-accessible pores, detects open pores ranging from about 1 to 350 nm, and quantifies their volume distribution. The three electron microscopy techniques provide visual and qualitative information on pore shape, size, aspect and 3D orientation at operator-selected locations in the specimens, and cover length scales from microns to nanometers. One important result obtained from gas adsorption is that densification of graphite irradiated before turnaround does not cause detectable changes in BET surface area and pore volume. This is an indirect confirmation of the accepted mechanism according to which densification before turnaround affects large accommodation pores, with little consequence on BET surface area. In contrast, graphite swelling after turnaround causes massive development of narrow mesopores (5–20 nm) which correlates with up to five times increase of BET surface area. Microscopy results confirmed consistently that severe structural changes occurred after turnaround. Moreover, the new electron microscopy images and raw adsorption isotherm data reported in this paper shed unique light on microstructure evolution in superfine grain graphite irradiated before and after turnaround, going up to doses of about 15 and 30 dpa. FIB-SEM tomography, TEM and gas adsorption data are also available as a Data-in-Brief communication.

Acknowledgments

This work was funded by a Nuclear Science User Facilities (NSUF) Rapid Turnaround Experiment (RTE) award. NSUF is the U.S. Department of Energy, Nuclear Energy Office's only designated nuclear energy user facility. A portion of this research used the resources of the Low Activation Materials Development and Analysis Laboratory (LAMDA), a DOE Office of Science research facility operated by the Oak Ridge National Laboratory (ORNL), and resources at the High Flux Isotope Reactor (HFIR), a DOE Office of Science User Facility operated by ORNL. Partial support from the Advanced

Reactor Technologies program of DOE Office of Nuclear Energy is also acknowledged. The authors are grateful to Tokai Carbon Co., Ltd. (Japan) for providing graphite grade G347A. Oak Ridge National Laboratory is managed by UT-Battelle under contract DE-AC05-00OR22725.

References

[1] W.P. Eatherly, Nuclear graphite – the first years, J. Nucl. Mater. 100 (1981) 55–63.
[2] A.L. Sutton, V.C. Howard, The role of porosity in the accommodation of thermal expansion in graphite, J. Nucl. Mater. 7 (1962) 58–71.
[3] J.E. Brocklehurst, B.T. Kelly, Analysis of the dimensional changes and structural changes in polycrystalline graphite under fast neutron irradiation, Carbon 31 (1993) 155–178.
[4] B.T. Kelly, T.D. Burchell, The analysis of irradiation creep experiments on nuclear reactor graphite, Carbon 32 (1994) 119–125.
[5] W. Windes, M. Davies, Design considerations for graphite in nuclear applications, International Nuclear Graphite Specialists Meeting (INGSM-16), Nottingham, UK, September 13-17, 2015.
[6] J.B. Spicer, L.E. Olasov, F.W. Zeng, K. Han, N.C. Gallego, C.I. Contescu, Laser ultrasonic assessment of the effects of porosity and microcracking on the elastic moduli of nuclear graphites, J. Nucl. Mater. 471 (2016) 80–91.
[7] H. Matsuo, The effect of porosity on the thermal conductivity of nuclear graphite, J. Nucl. Mater. 89 (1980) 9–12.
[8] C. Berre, S.L. Fok, B.J. Marsden, L. Babout, A. Hodgkins, T.J. Marrow, P.M. Mummery, Numerical modelling of the effects of porosity changes on the mechanical properties of nuclear graphite, J. Nucl. Mater. 352 (2006) 1–5.
[9] J. Kane, C. Karthik, D.P. Butt, W.E. Windes, R. Ubic, Microstructural characterization and pore structure analysis of nuclear graphite, J. Nucl. Mater. 415 (2011) 189–197.
[10] G.B. Neighbour, Modelling of dimensional changes in irradiated nuclear graphites, J. Phys. D Appl. Phys. 333 (2000) 2966–2972.
[11] B.T. Kelly, T.D. Burchell, Structure-related property changes in polycrystalline graphite under neutron irradiation, Carbon 32 (1994) 499–505.
[12] R.H. Telling, M.I. Heggie, Radiation defects in graphite, Phil. Mag. 87 (2007) 4797–4846.
[13] T. Tanabe, Radiation damage of graphite – degradation of material parameters and defect structures, Phys. Scripta T64 (1996) 7–16.
[14] W.T. Eeles, Small-angle X-ray scattering by pile-irradiated graphite, Nature 188 (1960) 287–288.
[15] N. C. Gallego, C. I. Contescu, T. D. Burchell, M. Kirkham, L. He, D. Changwoo, Annealing studies of irradiated HOPG using XRD and SANS measurements, International Nuclear Graphite Specialists Meeting (INGSM-16), Nottingham, UK, September 13-17, 2015.
[16] J.M. Dickinson, J.W. Shore, Observations concerning the determination of porosities in graphites, Carbon 6 (1968) 937–941.
[17] C. Karthik, J. Kane, D.P. Butt, W.E. Windes, Neutron irradiation induced microstructural changes in NBG-18 and IG-110 nuclear graphites, Carbon 86 (2015) 124–131.
[18] H.M. Freeman, A.N. Jones, M.B. Ward, F.S. HAge, N. Tzelepi, Q.M. Ramasse, A.J. Scott, R.M.D. Brydson, On the nature of cracks and voids in nuclear graphite, Carbon 103 (2016) 45–55.
[19] B.J. Marsden, G.N. Hall, O. Wouters, J.A. Vreeling, J. van der Laan, Dimensional and material property changes to irradiated Gilsocarbon graphite irradiated between 650 and 750 °C, J. Nucl. Mater. 381 (2008) 62–67.
[20] B.E. Mironov, J.M. Freeman, A.P. Brown, F.S. Hage, A.J. Scott, A V. K Westwood, J.P. Da Costa, P. Weisbecker, R.M.D. Brydson, Electron irradiation of nuclear graphite studied by transmission electron microscopy and electron energy loss spectroscopy, Carbon 83 (2015) 106–117.
[21] C. Karthik, J. Kane, D.P. Butt, W.E. Windes, R. Ubic, In situ transmission electron microscopy of electron-beam induced damage process in nuclear grade graphite, J. Nucl. Mater. 412 (2011) 321–326.
[22] J.A. Hinks, A.N. Jones, A. Theodosiou, J.A. van der Berg, S.E. Donnelly, Transmission electron microscopy study of graphite under in situ ion irradiation, J. Phys.: Conference Ser. 371 (2012), 012046.
[23] K.L. Jones, G.M. Laudone, G.P. Matthews, A multi-techniques experimental and modelling study of the porous structure of IG-110 and IG-430 graphite, Carbon 128 (2018) 1–11.
[24] E. Hoinkis, E. Robens, Surface area and porosity of unmodified graphite matrices A3-27 and A3-3 (1950) and oxidized matrix A3-3 (1950), Carbon 27 (1989) 157–168.
[25] E. Hoinkis, W.P. Eatherley, P. Krautwasser, E. Robens, Corrosion and irradiation-induced porosity changes of a nuclear graphitic material, J. Nucl. Mater. 141–143 (1986) 87–95.
[26] M.A. Banarez-Munoz, L.V. Flores Gonzales, J.M. Martin Llorente, Adsorption isotherms on nitrogen and argon on an "AGOT" grade artificial nuclear graphite at 77 and 90 K, Carbon 25 (1987) 603–608.
[27] M.A. Banarez-Munoz, J.M. Martin Llorente, L.V. Flores Gonzales, Textural study of a commercial pyrolytic graphite by physical adsorption of gases, Carbon 26 (1988) 681–685.
[28] S. Brunauer, P.H. Emmett, E. Teller, Adsorption of gases in multimolecular layers, J. Am. Chem. Soc. 60 (1938) 309–319.
[29] J.P. Olivier, M. Winter, Determination of the absolute and relative extents of basal plane surface area and "non-basal plane surface" area of graphites and their impact on anode performance in lithium ion batteries, J. Power Sources 97–98 (2001) 151–155.
[30] www.tokaicarbon.co.jp/en/products/fine_carbon/isotropic.html (accessed October 12, 2017).
[31] B. Khalaghim, H. Gudbrandsen, O.S. Kjos, K.S. Osen, T. Mokkelbost, G.M. Haarberg, In: E. Williams, T.M.S. (Eds.), Porous Carbon Anodes for the Supply of Methane during Electrowinning of Aluminum, Light Metals, vol. 2016, The Minerals, Metals & Materials Society, 2016, pp. 915–920, Table 1 and reference [13] Graphite & carbon specialistes [Online] http://en.tokaicarbon.eu/downloads/brochures.
[32] A.A. Campbell, Y. Katoh, M.A. Snead, K. Takizawa, Property changes of G347A graphite due to neutron irradiation, Carbon 109 (2016) 860–873.
[33] F. Rouquerol, J. Rouquerol, K.S.W. Sing, P. Llewellyn, G. Maurin, *Adsorption by Powders and Porous Solids*, second ed., Academic Press, 2014.
[34] J.P. Olivier, M. Winter, Determination of the absolute and relative extents of basal plane surface area and "non basal plane surface" area of graphites and their impact on anode performance in lithium ion batteries, J. Power Sources 97–98 (2001) 151–155.
[35] T. Placke, V. Siozios, R. Schmitz, S.F. Lux, P. Bieker, C. Colle, et al., Influence of graphite surface modifications on the ratio of basal plane to "non-basal plane" surface area and on the anode performance in lithium ion batteries, J. Power Sources 200 (2012) 83–91.
[36] E.P. Barrett, L.G. Joyner, P.P. Halenda, The determination of pore volume and area distributions in porous substances. I. Computations from nitrogen isotherms, J. Am. Chem. Soc. 73 (1951) 373–380.
[37] Z. Mileeva, D.K. Ross, D. Wilkinson, S.M. King, T.A. Ryan, H. Sharrock, The use of small angle neutron scattering with contrast matching and variable adsorbate partial pressures in the study of porosity in activated carbons, Carbon 50 (2012) 5062–5075.
[38] D.J. Baker, J.B. Morris, Structural damage in graphite occurring during pore size measurements by high pressure mercury, Carbon 9 (1971) 687–690.
[39] T.D. Burchell, Graphite: properties and characteristics, in: R.J.M. Konings (Ed.), Comprehensive Nuclear Materials, vol. 2, Elsevier, Amsterdam, 2012, pp. 285–305.
[40] K. Wen, T.J. Marrow, B. Marsden, Microcracks in nuclear graphite and highly oriented pyrolytic graphite (HOPG), J. Nucl. Mater. 381 (2008) 199–203.
[41] B. März, K. Jolley, T.J. Marrow, Z. Zhou, M. Heggie, R. Smith, H. Wu, Mesoscopic structure features in synthetic graphite, Mater. Des. 142 (2018) 268–278.
[42] N C Gallego, C I Contescu, T D Burchell, XRD and SANS evaluation of HOPG and polycrystalline graphite, ORNL/TM-2018/871; https://doi.org/10.2172/1458356.
[43] S. Ross, W. Winkler, On physical adsorption. VIII Monolayer adsorption of argon and nitrogen on graphitized carbon, J. Colloid Sci. 10 (1955) 319–329.
[44] S. Ross, W. Winkler, On physical adsorption. IX Sub-critical and supracritical adsorption isotherms for krypton monolayers on graphitized carbon black, J. Colloid Sci. 10 (1955) 330–337.